Fully integrated sample-in-answer-out platform for viral detection using digital reverse transcription recombinase polymerase amplification (dRT-RPA)

Seder, Islam; Coronel-Tellez, Rodrigo; Helalat, Seyed Hossein; Sun, Yi

Published in:
Biosensors and Bioelectronics

Link to article, DOI:
10.1016/j.bios.2023.115487

Publication date:
2023

Document Version
Publisher's PDF, also known as Version of record

Biosensors and Bioelectronics 237 (2023) 115487

Contents lists available at ScienceDirect

Biosensors and Bioelectronics

journal homepage: www.elsevier.com/locate/bios

Fully integrated sample-in-answer-out platform for viral detection using digital reverse transcription recombinase polymerase amplification (dRT-RPA)

Islam Seder, Rodrigo Coronel-Tellez, Seyed Hossein Helalat, Yi Sun *

Department of Health Technology, Technical University of Denmark, Ørsteds Plads, DK-2800, Kgs. Lyngby, Denmark

ARTICLE INFO

Keywords:
Isothermal amplification
Digital RPA
Viral diagnostics
Microfluidic fluid control

ABSTRACT

Recombinase polymerase amplification (RPA) is one of the most promising diagnostic methods for pathogen detection, owing to the simplified isothermal amplification technique. Using one-step digital reverse transcription RPA (dRT-RPA) to detect viral RNA provides a fast diagnosis and absolute quantification. Here, we present a chip that purifies, digitalizes, and detects viral RNA of SARS-CoV-2 in a fully automated and sensitive manner. The chip purifies the RNA using the surface charge concept of magnet bead-RNA binding, then mixes the RNA with the amplification reagents, digitalizes the amplification mixture, and performs dRT-RPA. RNA-bead complex is transported among purification buffers that are separated by an oil phase. For reagent manipulation and mixing, a magnetic valve system is integrated on the chip, where an external magnet controls the reagent direction and time of addition. Besides, a novel vacuum system is suggested to drive and regulate the reagents into two fluid systems simultaneously in ~2 min. We also developed a cost-effective way to perform fluorescent detection for dRT-RPA on chip by using EvaGreen® dye. With integrated heating and optical detection system, the on-chip dRT-RPA presents a sample-to-answer detection platform for absolute viral RNA quantitation in 37 min and a sensitivity as low as 10 RNA copies/μL. Hence, this platform is expected to be a useful tool for accurate and automated diagnosis of infectious diseases.

1. Introduction

During epidemics and pandemics, timely identification of the causative pathogen agent(s) is essential for disease surveillance, prevention, and treatment (Aileni et al., 2022; Cheung et al., 2022). Several diagnostic methods, including antibody/antigen and nucleic acids detection, are employed to provide a quantitative and/or qualitative assessment of pathogen presence (Chau et al., 2020; Vos et al., 2019). Although serological assays are simple and fast, the sensitivity and specificity of the diagnosis are low, especially during the early stages of infection (Kubina and Dziedzic, 2020). In contrast, nucleic acid amplification tests (NAATs), provide higher sensitivity and specificity (Areerob et al., 2023; Wang and Taubenberger, 2010). However, NAATs require sophisticated laboratory equipment, trained personnel, and preceding steps of nucleic acid purification from patient specimens prior to the amplification. Microfluidic technology postulates promising platforms to perform NAATs that involve a series of reagent and microbeads handlings and require temperature control and assessment with optical instruments (Jamiruddin et al., 2022; Kang et al., 2022). To perform fluid control and thermal amplification in a single platform, complex orchestration of the microfluidic components and heating system are obvious (Liu and Lee, 2022), which hinders the wide use of such platforms. Thus, there is a need for a simple, precise, and fully automated sample-in-answer-out NAAT-based detection platform.

One potential approach to simplify the microfluidic platforms is to use isothermal amplification methods such as loop-mediated isothermal amplification (LAMP) and recombinase-polymerase amplification (RPA), instead of the cyclic temperature process of polymerase chain reaction (PCR) (Augustine et al., 2020; Bai et al., 2022). Although PCR remains the “gold standard” method for bacterial and viral detection, it requires a bulky thermal apparatus to operate cyclic temperatures. Moreover, PCR operates at high temperatures, causing a serious reagent evaporation issue when performed on a chip (Polini et al., 2010). Isothermal amplification techniques have become efficient and sensitive alternatives to PCR (Zhu et al., 2020). Isothermal amplification provides a simplified diagnosis since it requires a single and lower temperature

* Corresponding author.
E-mail address: suyi@dtu.dk (Y. Sun).

https://doi.org/10.1016/j.bios.2023.115487
Received 24 April 2023; Received in revised form 2 June 2023; Accepted 15 June 2023
Available online 16 June 2023

with a short turnaround time. RPA, particularly, provides a versatile and efficient option since it only requires two oligonucleotides, it operates at low temperatures (37°C–42°C), and the amplification process can be monitored by adding fluorescent reporters (Augustine et al., 2020) such as exo-probes (TwistDx™), which are widely used due to their specificity (Dorendorf et al., 2022; El Wahed et al., 2021), although their design is complex and expensive, and the obtained amplification products are rapidly degraded. Furthermore, digital RPA (dRPA), wherein a positive fluorescent signal is distinguished from a negative within droplets or compartmentalized reactions can be developed using a microfluidic device, and it enables absolute quantification of pathogen nucleic acids (Baker, 2012). Such advantages enable its implementation on portable and automated chips with minimal cost, complexity, and running times. For viral RNA amplification, an additional step of reverse transcription (RT) is required, therefore, performing a one-step dRT-RPA in a single chip combined with a simple and cost-effective fluorescence-based detection system, would significantly facilitate the overall diagnostic process. However, to date, such a system has not been implemented on a microfluidic device.

To further simplify microfluidic systems and reduce on-chip components and off-chip controllers, some works have suggested passive components instead of the traditional active valve and mixers (Narayanamurthy et al., 2020; L. Xu et al., 2020). While such passive components successfully achieved some fluid control functions, lengthy and limited-step processes are obvious. Surface modification to obtain hydrophilic/hydrophobic valves and pumps, that are used to control fluid, lacks robustness and manifests time-dependent process (Hussain et al., 2023). Centrifugal disc achieved sample–to-answer detection (Sunkara et al., 2021), however, bulky motor, multi-valves on the chip, and complex design are presented. Using magnetic beads to capture and manipulate biomolecules (*e.g.*, nucleic acids) reduces the dependency on off-chip controllers since a single magnet is required as demonstrated in the rotational chip (Seder et al., 2021) and immiscible phase DNA/RNA isolation (Chen et al., 2020; Strotman et al., 2012). While integrating nucleic acid purification on the chip is advantageous over a laborious and prone-to-contamination manual process, extra steps, thus controllers, are required on the chip. Expanding the use of the external magnet to perform extra control functions such as valve or pump control on microfluidic chips would further reduce the number of off-chip controllers and simplify the sample to answer microfluid platforms.

For reagent digitalization and nucleic acid amplification, it is required to physically separate the reagent in nanoliter volumes. This is achieved by generating aqueous droplets in the oil phase (Choi et al., 2023; He et al., 2021) or reagent partitioning within a group of physical constraints (microwells) (Baker, 2012). Droplet-based digitalization on microfluidic chips requires bulky syringe pumps with the difficulty of droplet size optimization and significant reagent waste (He et al., 2021). Instead, reagent partitioning in microwells enables a more reliable digital amplification. Compartmentalization of the amplification reagent is achieved by applying a negative pressure (vacuum) to enable a dead-end microarray filling (Si et al., 2020; Wu et al., 2017; G. Xu et al., 2020). A vacuum chamber is traditionally used for degassing (creating a negative pressure) prior to the detection (Si et al., 2020). This adds an extra step for the end-user and creates result variation and a lengthy filling time because the array filling time is a function of a non-linear decrease of the negative pressure. Vacuum battery (pre-stored vacuum on a chip) is suggested to eliminate the need for the vacuum chamber (Yeh et al., 2017), however, this vacuum battery requires a complex structure, a reliable storage system, and a lengthy filling time. Short filling time is crucial in dRPA since the amplification starts directly after mixing the reagents with the RPA initiator, while some works achieved ~2 min filling time with parallel-channel system by using several external syringe pumps (Yin et al., 2020; Zhou et al., 2019), it fails to fill the oil-phase uniformly using a single vacuum source due to the difference in hydraulic resistance among parallel channels. Thus, developing a fast and simple vacuum system for digitalization is essential for dRPA.

In this work, we present a sample-in-answer-out platform that integrates immiscible phase nucleic acid isolation and digital RT-RPA for viral RNA detection. The platform simplifies the RNA purification and reagent addition and mixing process by using a single external magnet to control RNA-bound magnetic beads. The pure RNA is then mixed with the RT-RPA mixture by a magnetically driven valve prior to reagent digitalization with a vacuum system (Fig. 1). The suggested valve provides sophisticated mechanical control for the fluids without adding additional off-chip controllers. To rapidly fill the microwell array, we developed a new vacuum system that uses a single vacuum source to drive the reagent into two systems: microwell and main channel, simultaneously, and compartmentalize the reagent by an oil phase. We also successfully employed EvaGreen® fluorescent reporter dye for dRT-RPA as a simple and cost-effective alternative to exo-probes, with strong and specific amplification signals. Our proposed system transports, mixes, and digitalizes reagents, and performs dRT-RPA in 37 min; an absolute quantification of viral RNA is achieved on-chip without compromising any step during the purification and amplification processes in a fully automated and precise manner. To the best of our knowledge, this is the first work to implement RNA purification and dRT-RPA on-chip, resulting in a reliable and accessible platform that can be used for timely pathogen detection in point-of-care settings.

2. Material and methods

2.1. Device structure

The disposable device consists of three sections: nucleic acid (RNA) isolation section that has open chambers, a fluid control system that contains a magnetic valve and a passive mixer, and a microwell section for dRT-RPA (Fig. 2a). The RNA isolation section contains 6 open chambers for cell lysis (C1), RNA washing (C2–C3), RNA elution (C4), RT-RPA mixture (C5), and mineral oil (C6). Mini-chambers that contain mineral oil are used to separate the buffers in C1–C4 (Fig. 2b). The fluid control section includes a magnetically driven rotational valve that directs the reagent from C4–C6 to the mixer prior to reagent digitalization in the microwell section (Fig. 2c). A mini-stepper motor is placed under RNA isolation and fluid control sections to control the movement of the external magnet. Last, the microwell section (Fig. 2d) consists of 3 layers: a bottom layer that has the microwells for dRT-RPA, a middle layer that consists of air permeable membrane for degassing the microwells, and a top layer for the vacuum system (Fig. S1). Another mini-stepper motor is placed beside the chip to generate a negative pressure in a small syringe, that is connected to the vacuum layer. A heater unit is placed under the microwell section. For optical detection systems, a fluorescent light source and detection are mounted on the top of the device.

2.2. Operational process for viral RNA amplification

The platform automatically performs the entire process including RNA purification from viral-containing samples and dRT-RPA (Fig. 2). Before the device operates, reagents are stored into chambers C1–C6 as follows: 50 μL lysis buffer-bead mixture (C1), 50 μL washing buffer (C2–C3), 6 μL elution buffer (C4), 35 μL RT-RPA mixture (C5) and 20 μL mineral oil (C6). 17 μL of sample is loaded in the only open chamber (C1-the lysis chamber). The sample is composed of phosphate-buffered saline (PBS), or human swab viral collection medium (Viral collection and transport kit, Meditec Inc.) spiked with 1 μL of RNA. See loading process in Fig. S2. To prevent contamination of the platform, C1 can be closed by a glass slip or a plastic cap after loading the sample.

For RNA purification (Fig. 2b), in step 1, magnetic beads (MB) are added to C1 to bind with the RNA in the lysis/sample mixture. In step 2, with the aid of a magnetic disc, the MB-RNA complex is transferred to C2 for the first wash and then to C3 for the second wash. During this process, the MB-RNA complex goes through the mineral oil phase in the

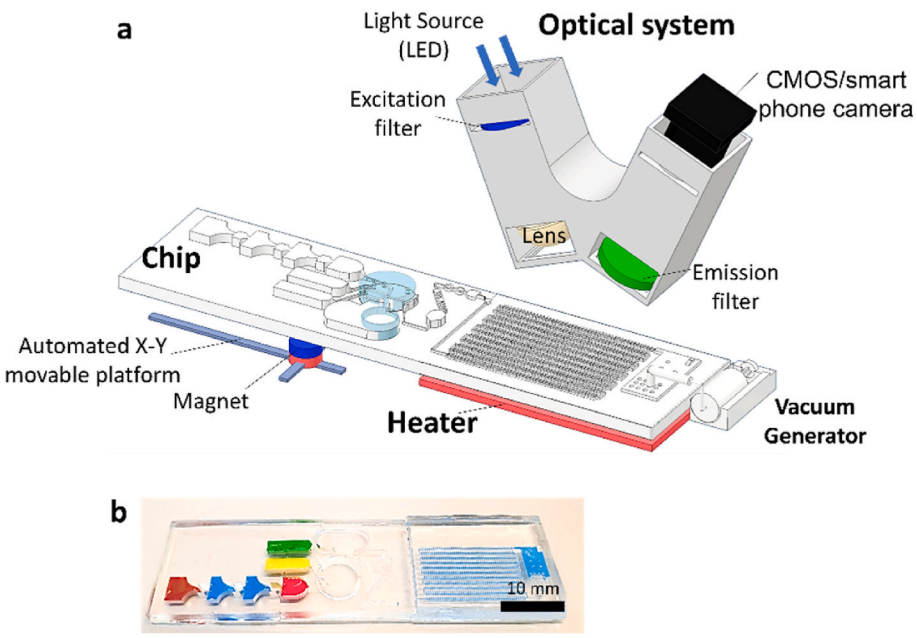

Fig. 1. Microfluidic platform for sample-to-answer digital RT-RPA. (a) Schematic illustration of the total system consisting of a magnetic platform, heater unit, vacuum generator, detection part with camera, and light-emitting diode (LED). The disposable chip has three operational zones to prepare and mix the reagents and detect the pathogen agent. (b) Dye-loaded chambers for visualization of chips. Brown, blue, and red show lysis, washing and elution chambers, respectively, for sample preparation. Green and yellow chambers show RPA mixture and mineral oil chambers, respectively.

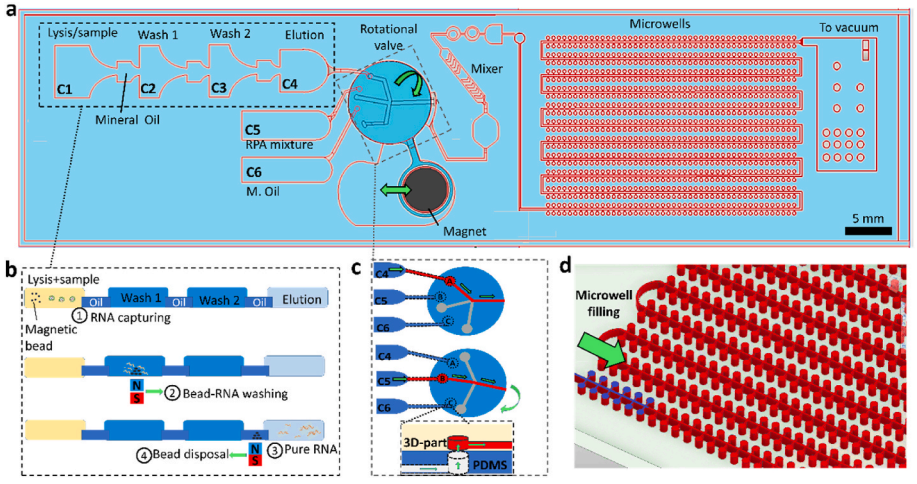

Fig. 2. Schematics illustrating of the chip operational process. (a) The chip consists of three zones for sample preparation, reagent mixing and digital amplification The sample preparation process, that is based on immiscible phase separation of isolation buffer, is composed of 3 steps including lysis in (C1), wash in (C2–C3) and elution in C4. (b) Once the user loads the sample in C1, RNA binds with magnetic beads. Magnetic bead-RNA complex is transported through the washing buffers to elution buffer by the aid of external magnet. (c) In zone 2, the purified RNA (C4) and RPA mixture (C5) are dragged and mixed by the aid of negative pressure in the channel. A rotational valve regulates the time and volume of reagent addition to the mixer. (d) lastly, the mixture of RNA and RT-RPA reagents enters the microwells for reagent digitalization. The volumes used for reagents were as follows: 67 μL viral sample, lysis and beads (C1), 50 μL for washing (C2–C3), and 6 μL elution buffer (C4), 35 μL RT-RPA mixture (C5), 20 μL mineral oil buffer (C6).

mini-chambers. In step 3, the MB-RNA complex is transferred to the elution buffer (C4), wherein MB is separated from the RNA, resulting in a pure RNA. The wasted MBs are transferred back to C3 in step 4. The bottom magnetic disc moves in X and Y dimensions to improve the MB-RNA binding and mixing in steps 1–3. The pure RNA in C4 is now ready to be mixed with the RT-RPA mixture. The process is shown in Movie S1.

To add and mix the purified RNA and RT-RPA mixture, stepper motor 2 creates a vacuum in the channels and the mixing zone, driving the solution from C4 (RNA) into the mixing section. After a certain period, the valve rotates clockwise (CW) to allow a portion of the RT-RPA mixture in C5 to go into the mixer channel (See movie S2). Fig. 2c demonstrates that by alternating the valve opening between valve pathway A and valve pathway B at a certain opening time, the volume ratio between the RNA in C4 and the RT-RPA mixture in C5 can be precisely controlled. After the combination of RNA with RT-RPA reagents in the mixing area, the reaction mixture keeps moving to the microwell section to fill the microwells (Fig. 2d). Then, the valve rotates CW to open pathway C to allow the mineral oil in C6 to pass through the mixture region and digitalize the RT-RPA reaction mixture in the microwells (See Movie 3). Subsequently, the bottom heater is switched on and maintained at 42 °C for 25 min to perform RT-RPA. Finally, the fluorescent signal of the RT-RPA-amplified RNA products is obtained by light excitation using LEDs while a digital image is taken of the microwell section for post-analysis. To prevent contamination, we used a new syringe for the vacuum generator for each test. Additionally, the PDMS membrane provides a physical separation between the vacuum generator and the reagent in the device.

2.3. Device fabrication

The platform consists of permanent (reusable) parts and a disposable chip. The permanent parts are the magnetic support, the heating and optical systems, and the vacuum generator. The disposable chip was fabricated from Polydimethylsiloxane (PDMS). Details of the fabrication process are found in SI and Fig. S3.

2.4. Experimental setups

The heater, excitation light source, and camera are shown in Fig. 1 and Fig. S4. The light source (wavelength of 495 nm) and the camera/

smart phone were used to excite and monitor the RT-RPA amplification, respectively. The detailed set-up for the optical and heating system and control of the motors are found in SI including circuit connection (Fig. S5) characterization of the mixing efficiency and RNA isolation efficiency (Fig. S6). To calculate the relative standard deviation (RSD), we divided the standard deviation of a data set to the mean of the data set and multiply it by 100.

2.5. Fluorescence imaging and dRT-RPA quantification analysis

A fluorescent signal was produced when EvaGreen® dye was activated after binding to the double-stranded DNA (dsDNA) generated during amplification. EvaGreen® dye was excited at 498 nm, and the fluorescent signal was proportional to the dsDNA present in the reaction. Images of the fluorescent amplification signal were acquired using ThorCam software, wherein the contrast of images was adjusted and applied equally for all tests. The raw CMOS camera images were in gray scale while the smartphone images were colored. ImageJ software was used for the post-analysis of fluorescence intensity and brightness adjustments.

2.6. Viral RNA samples and RNA purification reagents

Synthetic RNA controls of SARS-CoV-2 (MN908947.3, Wuhan-Hu-1) and Influenza A H1N1 (NC_026431-NC_026,438) were used in this work, and they were obtained from Twist Bioscience. A commercial RNA Purification Kit (MagMAX™ Viral RNA Isolation Kit, Applied Biosystems), which includes the magnetic beads, and the lysis, wash, and elution buffers, was used for RNA purification. Purified RNA was obtained in 6 μl of elution buffer. To characterize the extraction performance, we used a commercial PCR machine (C1000 Touch Cycler, Bio-Rad).

2.7. One-step RT-RPA experimental conditions

The TwistAmp® Liquid Basic kit (TwistDx) was used for isothermal amplification with the volume of the kit reagents adjusted for a final reaction volume of 34 μL. 0.7 μL of forward and reverse primers at a concentration of 10 μM were employed. Primer sequences are shown in Table S2. 1.4 μL of SuperScript™ IV Reverse Transcriptase (280 U, ThermoFisher) and 1.4 μl of RNase inhibitor (28 U, Applied Biosystems) were added for reverse transcription of viral RNA. Additional reagents included: 1 μL of EvaGreen® 20X dsDNA-intercalating dye (Biotium) as the fluorescent reporter, 1.4 μl of DMSO 100% to decrease the formation of undesired double-stranded DNA products, and 1.4 μL of DTT 0.1M to ensure the adequate function of the enzymes involved in the reverse transcription and amplification reactions (Euler et al., 2012). 34 μL of RT-RPA reaction mix were combined with 6 μl of isolated viral RNA prior to digitalization and one-step dRT-RPA process at 42 °C.

3. Results and discussion

3.1. Nucleic acid purification

Nucleic acid (*i.e.*, RNA) was isolated based on the immiscible phase barrier concept (surface tension valve), wherein, two aqueous phases are separated by the oil phase due to interfacial tension difference (Strotman

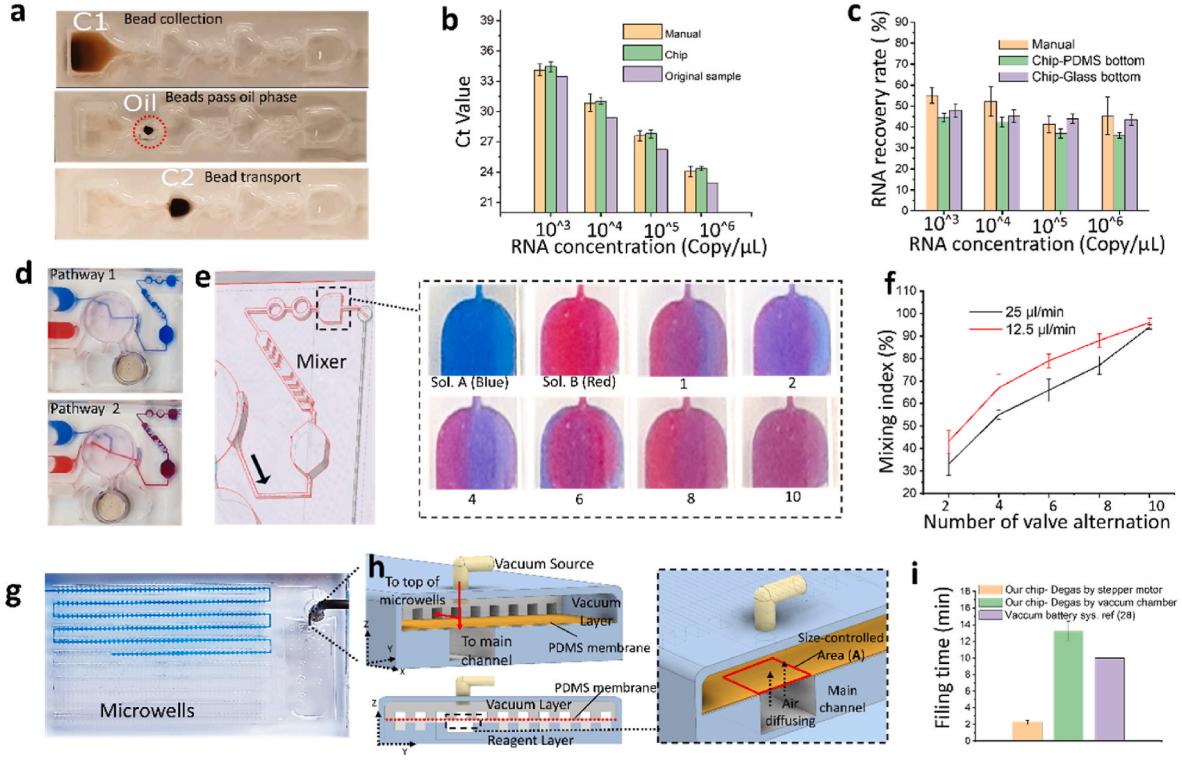

Fig. 3. Nucleic acid purification and reagent manipulation. Error bars are SD. for n = 3. (a) Steps of nucleic acid purification using immiscible phase barrier. RNA-bead complex transportation/manipulation through nucleic acid purification buffers. (b) Performance of RNA isolation on the chip compared with manual isolation off-chip. RSD: 0.42 ± 0.081%. (c) Recovery of RNA using the surface tension valve method. RSD: 6.5 ± 2.4%. (d–f) Fluidic control of the reagents using a magnetically actuated rotational valve. (d) Real images of RV showing two states of the valve. (e) Passive mixing unit. The inset shows real images during the mixing process. The number below the images represents the number of valve alterations between solution A and B per test (f) The influence of valve alternation on the mixing efficiency. (g) Image of the microwell filling using a vacuum. Fluid fills the microwell and flows in the main channel, simultaneously. Food-dye color for visualization. (h) The single vacuum source is distributed into two sections: microwells and main channel to pump fluid by air diffusion over the permeable membrane. The inset shows the size-controlled area (A) of membrane. Filling speed in the main channel is controlled by A (i) comparison of the reagent filling time for different vacuum systems for 100 μL. RSD: 0.8 ± 0.09%.

et al., 2012). Thus, the aqueous phases of nucleic acid purification reagents such as lysis, wash, or elution buffers, do not mix with each other, meanwhile, solid magnetic beads are allowed to travel smoothly among the phases. Through experimentation and inspired by previous works (Chen et al., 2020), we chose the shape of the chambers and found that the oil phase can be contained in mini chambers between the RNA purification reagents. Detailed dimensions of the chamber are shown in Fig. S7. The RNA purification region was constructed from four chambers (C1–C4) and separated by 3 mini-chambers that contain oil (Fig. 3a). Although in this work synthetic RNA was used as the starting sample, initially, viral-containing cells from clinical samples can be lysed in C1 and then, total RNA binds to the magnetic beads. After 30 s, the RNA-bound magnetic beads were transferred through the oil phase to C2 for the first washing (Fig. 3a). The washing process takes 30 s and then it is repeated in C3 to ensure RNA purity. Finally, the RNA-MB complex is transferred to C4 to elute the RNA from the beads (1 min). Magnetic beads were then transferred and discarded in C3, leaving C4 with pure RNA. The external magnet moves in X and Y dimensions to tightly control bead manipulation and improve all the steps during RNA purification. We assessed the RNA purification process using RT-qPCR, where the obtained Ct value was plotted against 4 serial dilutions of spiked RNA in the lysis mixture (Fig. 3b). The purified RNA on the chip was compared with manual purification. The results in Fig. 3b show that the purification on chip underperforms the manual purification, as the Ct value is higher for the RNA purified on the chip (RSD: 0.42 ± 0.081% and n = 3). The lower efficiency (higher Ct value) of the chip purification can be attributed to some loss in RNA-bound magnetic beads during the phase-to-phase transporting. We noticed that a daughter droplet was created, and some remaining magnetic beads were left in the previous chamber when the MB-RNA complex passed through the oil phase during the purification (Fig. S8). Many works have attempted to solve such phenomena by using a surfactant to reduce the surface tension among aqueous and oil phases (Troiano et al., 2017) or using different material properties for the bottom of the chip (Adams et al., 2013; Metzler et al., 2020). Because this is out of this work scope, we simply replaced the bottom layer of the chip with a glass slide instead of PDMS and repeated each step of MB-RNA transporting to enhance the purification efficiency. Fig. 3c shows the purification efficiency improved from 39% to 46% (RSD: 6.5 ± 2.4% and n = 3). after replacing the bottom material with glass, which was comparable to manual purification. Thus, the yield of RNA purified on the chip is adequate for the subsequent amplification process. We also spiked synthetic RNA in the human nasal swab and performed the detection (Fig. S9). Yield of RNA shows a similar Ct value for RNA in PBS buffer and RNA spiked in nasal swab samples.

3.2. Workflow and reagent manipulation

The pure RNA needs to be mixed with RT-RPA mixture prior to reagent digitalization in microwells, thus, we designed a fluid system that enables the chip to bring and mix two (or more) solutions together in a precise and automated manner without adding an external controller. Initially, we have designed a single-layer magnet valve that permits the RNA and RPA mixture to pass to the mixer zone; however, leakage appeared in several spots (Fig. S10). Thus, we introduced a two-layer rotational valve that is composed of PDMS and 3D-printed parts to prevent leakage (Fig. 3d). First, solution A in C4 enters an open pathway of a valve on the way to the mixer zone due to the negative pressure in the microwells (See Fig. 3d and Movie 2). Second, to bring solution B in C5, the rotational valve (RV) rotates 30-degree CW to close pathway 1 and open pathway 2. Now, solution B in C5 is driven into the mixing zone. Finally, to bring solution C from C6, pathway C is enabled by rotating the RV 30-degree CW. The valve motion was activated with the aid of the external magnetic, wherein the translation motion of the magnet creates a torque on the valve, thus rotating it.

The top layer of the RV was designed with a 3D-printed part for two reasons: 1) To provide strength for the RV to sustain the torque generated by the magnetic force at its arm. 2) The interaction between the 3D-printed surface of the RV and the PDMS material of the bottom layer provides a smooth motion for the RV, while the flexibility of the PDMS material assures a perfect gasket to prevent leakage between the 3D-printed RV and chip PDMS surface. Studies of rigid-to-rigid bodies interface showed a necessity for mineral oil (Yu et al., 2020) or an extra flexible membrane to prevent leakage (Seder et al., 2022), while PDMS-PDMS surfaces make the valve motion sticky according to our experimentation. Thus, we achieved smooth rotational motion and fluid control for 3 reagents in C4–C6. It is worth mentioning that assuring tight contact between the PDMS surface and the 3D-printed RV is crucial to prevent fluid leakage on the RV. Details of RV dimensions are shown Fig. S7.

To improve the mixing between the RNA and RT-RPA mixture, a passive mixer route, inspired by (Stroock et al., 2002) was designed prior to microwell compartmentalization. We also alternated the opening of pathways 1 and 2 of RV to improve mixing efficiency. We used color dye to characterize the mixing efficiency between reagents in C4 and C5. Fig. 3e and f shows that as the number of pathway alternations increased in a fixed total time of filling (120 s), the mixing efficiency continuously increased. For instance, with 2-alteration/120 s, the mixing efficiency was >35%, whereas the mixing efficiency reached 92% at10-alternation/120 s at 12.5 μL flow rate (RSD: 4.6 ± 0.8% and n = 3). This mixing improvement can be directly attributed to a bigger interface between the two reagents (dye 1 and dye 2) throughout the mixer route. We applied the aforementioned fluid control concept on the chip to mix the elution buffer that contains the purified RNA in C4 and RPA mixture in C5 at 10-time alternations during the filling time. After RNA elution and RT-RPA mixture are combined and mixed in the mixing zone, they pass to the amplification section and start filling the microwells. Finally, the mineral oil in C6 is permitted to go through the amplification channels and digitalize the RT-RPA reaction mixture by rotating the RV 30-degree CW to open pathway 3. Because the rotational valve changes the pathways from one to another, the exiting air in the empty channels appears in the pathways, however, air is eliminated by the steady and gentle action of the vacuum system. Thus, the presence of small air bubbles is temporary, and it does not interfere with the performance of sequential steps. Unlike some works in which the mixing step is compromised and the valves were activated manually (Yin et al., 2020; Zhou et al., 2019), our chip integrated an automated valve and passive mixer. We believe these components are essential to ensure simple and homogeneous mixing for outstanding RT-RPA performance.

3.3. Vacuum system

Microwell filling and compartmentalization play a crucial role in the performance of digital amplification on a chip. Fast and complete filling assures accurate reading since the reagent digitalization must start before the beginning of amplification. Some works pre-stored the RPA initiator or the RPA mixture in the microwells during the chip fabrication to avoid pre-amplification (Yeh et al., n.d.; Yin et al., 2020) because reagent digitalization takes >10 min. However, rapid reagent digitalization (<2 min) prevents pre-amplification. Thus, in our suggested vacuum system, we designed a reagent filling system that prioritizes the speed of filling (Fig. 3 g-i). To drive the solution in the chip in a fast manner, we found in the literature that vacuum generation using a syringe pump provides the strongest negative pressure, thus fast performance. However, to avoid using a bulky syringe pump to generate negative pressure, we integrated a mini stepper motor to create a vacuum in a syringe that is connected to the chip. The generated vacuum is divided into two systems: above the microwells and at the end of the main channel to drive the reagents into both systems, simultaneously (Fig. 3g and h). This vacuum division allows controlling the velocity of the reagent filling without the need to use a multi-vacuum source. Thus, the microwells will be filled with the RT-RPA while it still flows in the

main channel. Later, the mineral oil will flow into the main channel for digitalization (Movie S3). The magnitude of the vacuum in the main channel regulates the flow velocity in the channels and the mixer. If the vacuum is too strong, the reagent reaches the end of the main channel before it completely fills the microwells. If the vacuum is too weak, a slow filling time (F_t) is observed. Thus, to control the reagent velocity in the main channel, we applied a strong vacuum (70 kPa) while varying the membrane area (A) that separates the top vacuum chamber and the bottom channel (See the inset of Fig. 3h). Thus, the amount of air that diffuses between the top vacuum area and the bottom main chamber is precisely controlled. Thus, by optimizing A, an efficient filling can be obtained. We found that at A = 11 mm^2, the filling of the microwells and the main channel results in the shortest and more efficient filling time. For example, with a large A (20 mm^2), the vacuum system provides a fast-filling time ($F_t < 2$ min) in the main channel; but this fast filling is at the expense of incomplete filling in the side microwells. With a small A (5 mm^2), filling in microwells is complete, however, the velocity of the reagent in the main channel is slow ($F_t > 4$ min) causing a delay in the filling process. Thus, this vacuum configuration system requires a single vacuum source without the need for extra valves (Zhou et al., 2019) or several vacuum generators (Yin et al., 2020).

The suggested generated vacuum on the chip system provides a fast (~2 min), robust and simple filling because (i) a strong and constant vacuum is possible with the mini stepper motor; (ii) an automated pressure generator eliminates the variation and incubation time uncertainty that exists in the vacuum chamber systems; (iii) only a single vacuum source is required to drive two different flow paths. As shown in Fig. 3i, our vacuum system (negative pressure generation on the chip) shows clear advantages when compared to the conventional vacuum chamber, and vacuum battery (Yeh et al., n.d.). The vacuum chamber and the vacuum battery need longer filling time due to a bulky PDMS layer to diffuse the air and a limited magnitude of stored negative pressure, respectively. Moreover, both vacuum systems display flow rate decay while our vacuum system keeps the vacuum at constant magnitude during the whole process (Fig. S11).

3.4. Absolute RNA quantitation by dRT-RPA

To quantitatively determine the RT-RPA performance on-chip, we spiked synthetic SARS-CoV-2 RNA with a known copy number into the lysis chamber (C1). Fig. 4 shows the quantitative amplification performance of the chip with four serially diluted SARS-CoV-2 RNA samples whose concentrations ranged from 10^4 to 10 copies/μL. As the RNA concentration of the spiked sample was diluted, the number of positive microwells (fluorescent signal) decreased, while the reaction without RNA showed no fluorescent signal (Fig. 4e). The absolute RNA quantitation was obtained from the count of positive microwells relative to the entire number and volume of microwells. Thus, dRT-RPA provides a straightforward quantitative assessment of the initial copy number of RNA, since the assessment depends on sample dilution, the total number of microwells, and the performance of RNA isolation. However, because there is a possibility of existing more than one template RNA in a given microwell that can lead to underestimating the true initial RNA copy number, we used a Poisson correction to determine the relationship between the expected and the observed copy number of the template RNA (Fig. 4g). Poisson correction was used since the template RNA distribution is random (Song et al., 2015; Zhou et al., 2019). Detailed calculations for dRT-RPA assessment can be found in SI. Fig. 4g shows that the detected number of positive microwells has a good correlation with the expected positive microwells (R = 0.998). Although the observed positive microwells in Fig. 4a–e shows a slight variation from those expected theoretically the trend of increasing positive microwells in relation to the RNA concentration of the spiked sample shows a clear consistency. Thus, the presented sample-to-answer dRT-RPA chip can precisely quantify the initial RNA copy number in each sample. Moreover, to confirm that the observed signals are not false positives, we performed gel electrophoresis of RT-RPA products and confirmed that in all cases, an amplification product with the expected size of 195 bp was obtained (Fig. S12).

To examine the specificity of dRT-RPA, we tested the chip with Influenza A virus (Inf. A). We spiked synthetic Inf. A RNA in the lysis-MB mixture, and carried out the entire purification and RT-RPA process on the chip. No microwells with fluorescent signals were observed after the amplification reaction, demonstrating an adequate specificity of the dRT-RPA process on-chip. These results indicate that the designed dRT-RPA system can accurately detect specific viral RNA target when suitable primers are employed.

Using EvaGreen® as the RT-RPA fluorescent reporter instead of an exo-probe, provided a strong amplification signal with significant cost reductions. Exo-probes, although specific, are highly expensive, and can be used for a single target, while accessible and "universal" fluorescent dyes such as EvaGreen® can be used for any number of specific dsDNA targets with a highly stable signal. Nevertheless, just a few studies have used fluorescent dyes to monitor RPA amplification (Lai and Lau, 2020; Zheng et al., 2021), probably due to the possibility of obtaining background fluorescent signals from the activation of the dye after binding to unspecific dsDNA. However, in this study, after optimization of the RT-RPA conditions on-chip and design of specific primers, no unspecific fluorescent signal was observed in our tests. Furthermore, the strong fluorescent signal of EvaGreen® enables our simple optical system of

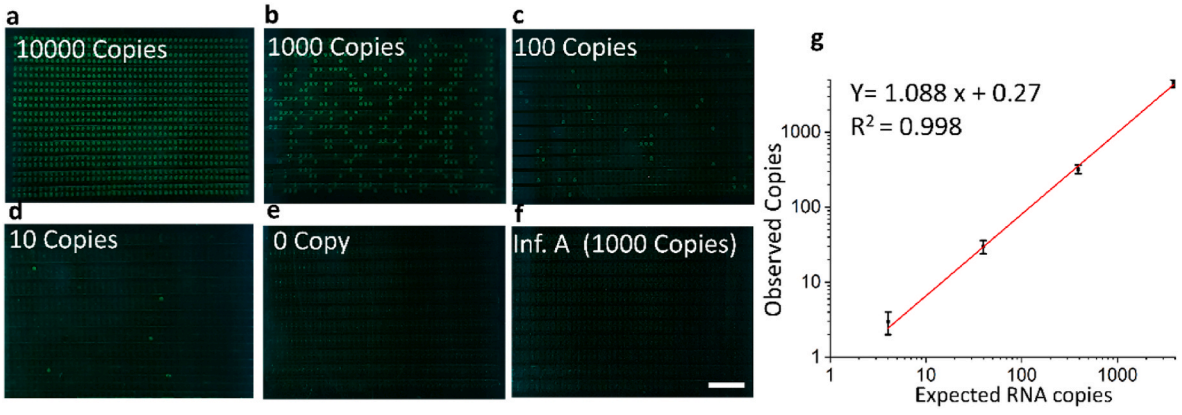

Fig. 4. Quantitative performance of the integrated chip with different concentration of SARS-CoV-2 RNA. Error bars are SD. for n = 3. (a)–(e) RT-Digital RPA with a serial dilution of target RNA template ranging from 10^4 copies/μL to 0 copies/μL. (f) The specificity assay using Inf. A with 10^3 copies/μL. The scale bar is 3 mm. (g) The linear regression curve (R^2 = 0.996) between the expected copy number per reaction and the observed copy number. The data are expressed as mean +standard deviation.

LEDs and smartphone to provide direct assessment for dRT-RPA with high sensitivity. Compared to the traditional RT-qPCR and exo-probe-based RT-RPA, our developed chip provides an absolute and sensitive quantitative assessment using dRT-RPA in a one-step process without using bulky, complex, and/or expensive systems.

Although some commercially available devices employing isothermal amplification to detect SARS-CoV-2 display a satisfactory limit of detection (LOD) and less than a 10 min process (*e.g.*, ID NOW™ COVID-19 2.0, Abbott and Metrix COVID-19 Test, Aptitude Medical Systems Inc) as well as some microfluidic devices such as sample-to-answer RT-LAMP chip (Song et al., 2023) that provides LOD of 0.5 copies/μL in 20 min, none of these systems perform an absolute quantification of the viral RNA copies. Other similar sample-to-answer devices achieved an absolute nucleic acid estimation for DNA with LOD of less than 10 Copy in 45 min (Yin et al., 2020), however, our device presents, for the first time, a viral RNA detection on digital platform using RT-RPA. Besides, unlike our suggested platform, most of the current digital chips use a commercial fluorescent reading system after the amplification adding additional equipment to the detection process Although the chip was fabricated from a PDMS material with less than a 3 USD/chip, mass production of the device (*e. i.* top and bottom layers) is feasible since the size feature of the device is approachable in cheap and fast manufacturing processes such as plastic extrusion or injection molding. The middle layer of PDMS membrane can be assembled with large number of the top and bottom layers simultaneously for rapid production.

4. Conclusions

The presented chip achieves a full viral diagnostic test in an automated manner with the least number of off-chip controllers and without compromising any isolation and amplification step. This platform enables digital RT-RPA in an inexpensive, simple, and accurate form. The control for bead manipulation and reagent addition and mixing are achieved using a single external magnet. For reagent digitalization, the newly suggested vacuum system permits a fast reagent filling into 1012 microwells in ~2 min. The chip performs several control functions precisely with only two cheap and simple mini stepper motors instead of a bulky and complex control system. The findings provided proof-of-concept that using dRT-RPA with EvaGreen® dye expedites the diagnosis and provides an absolute and sensitive quantitative assessment for of SARS-CoV-2. The suggested magnetic valve and vacuum system were used successfully to control one simple flow on the chip. Increasing the number of workflows in applications that require several reagents would create a challenge for the suggested designs. Thus, expanding the search on such systems enables multi-target detection or multi-step immunoassays such as ELISA. Additionally, exploring the use of EvaGreen® dye for RT-RPA with other viruses is an interesting area.

CRediT authorship contribution statement

Islam Seder: Conceptualization, Methodology, Investigation, Writing – original draft, Writing – review & editing. **Rodrigo Coronel-Tellez:** Methodology, Investigation, Writing – original draft, Writing – review & editing. **Seyed Hossein Helalat:** Investigation, Resources. **Yi Sun:** Conceptualization, Supervision, Writing – review & editing, Funding acquisition.

Declaration of competing interest

The authors declare the following financial interests/personal relationships which may be considered as potential competing interests: Yi Sun reports financial support was provided by Novo Nordisk Foundation.

Data availability

Data will be made available on request.

Acknowledgements

This work was supported by NovoNordisk Foundation, Exploratory Interdisciplinary Synergy Programme, Grant no. NNF21OC0070706.

Appendix A. Supplementary data

Supplementary data to this article can be found online at https://doi.org/10.1016/j.bios.2023.115487.

References

Adams, N.M., Creecy, A.E., Majors, C.E., Wariso, B.A., Short, P.A., Wright, D.W., Haselton, F.R., 2013. Biomicrofluidics 7 (1), 014104.
Aileni, M., Rohela, G.K., Jogam, P., Soujanya, S., Zhang, B., 2022. Cells 11 (7), 1182.
Areerob, Y., Sagadevan, S., Oh, W.C., 2023. Nanotechnol. Rev. 12 (1), 2022-0513.
Augustine, R., Hasan, A., Das, S., Ahmed, R., Mori, Y., Notomi, T., Kevadiya, B.D., Thakor, A.S., 2020. Biology 9 (8), 182.
Bai, Y., Ji, J., Ji, F., Wu, S., Tian, Y., Jin, B., Li, Z., 2022. Talanta 240, 123209.
Baker, M., 2012. Nat. Methods 9, 541–544.
Chau, C.H., Strope, J.D., Figg, W.D., 2020. Pharmacotherapy 40, 857–868.
Chen, Y., Liu, Y., Shi, Y., Ping, J., Wu, J., Chen, H., 2020. TrAC, Trends Anal. Chem. 127, 115912.
Cheung, P.H.H., Chan, C.P., Jin, D.Y., 2022. Emerg. Microb. Infect. 11 (1), 1072–1078.
Choi, J.W., Seo, W.H., Kang, Taejoon, Kang, Taewook, Chung, B.G., 2023. Lab Chip 23 (11), 2389–2398.
Dorendorf, A., Bachmann, I., Spiegel, M., Abd El Wahed, A., Dame, G., Hufert, F., 2022. J. Clin. Virol. 2, 100115.
El Wahed, A.A., Patel, P., Maier, M., Pietsch, C., Rüster, D., Böhlken-Fascher, S., Kissenkötter, J., Behrmann, O., Frimpong, M., Diagne, M.M., Faye, M., Dia, N., Shalaby, M.A., Amer, H., Elgamal, M., Zaki, A., Ismail, G., Kaiser, M., Corman, V.M., Niedrig, M., Landt, O., Faye, O., Sall, A.A., Hufert, F.T., Truyen, U., Liebert, U.G., Weidmann, M., 2021. Anal. Chem. 93, 2627–2634.
Euler, M., Wang, Y., Nentwich, O., Piepenburg, O., Hufert, F.T., Weidmann, M., 2012. J. Clin. Virol. 54, 308–312.
He, Z., Wang, J., Fike, B.J., Li, X., Li, C., Mendis, B.L., Li, P., 2021. Biosens. Bioelectron. 191, 113458.
Hussain, G., Jafry, A.T., Malik, S., Shah, S.F., Nishat, S., Awan, F.R., 2023. Sensor. Actuator. B Chem. 378, 133142.
Jamiruddin, M.R., Meghla, B.A., Islam, D.Z., Tisha, T.A., Khandker, S.S., Khondoker, M. U., Haq, M.A., Adnan, N., Haque, M., 2022. Life 12 (5), 649.
Kang, T., Lu, J., Yu, T., Long, Y., Liu, G., 2022. Biosens. Bioelectron. 206, 114109.
Kubina, R., Dziedzic, A., 2020. Diagnostics 10 (6), 434.
Lai, M.Y., Lau, Y.L., 2020. Acta Trop. 208, 105511.
Liu, W., Lee, L.P., 2022. Adv. Mater. 35, 2206525.
Metzler, L., Rehbein, U., Schönberg, J.N., Brandstetter, T., Thedieck, K., Rühe, J., 2020. Anal. Chem. 92 (15), 10283–10290.
Narayanamurthy, V., Jeroish, Z.E., Bhuvaneshwari, K.S., Bayat, P., Premkumar, R., Samsuri, F., Yusoff, M.M., 2020. RSC Adv. 10, 11652–11680.
Polini, A., Mele, E., Sciancalepore, A.G., Girardo, S., Biasco, A., Camposeo, A., Cingolani, R., Weitz, D.A., Pisignano, D., 2010. Biomicrofluidics 4, 036502.
Seder, I., Kim, D.M., Hwang, S.H., Sung, H., Kim, D.E., Kim, S.J., 2021. Sensor. Actuator. B Chem. 349, 130788.
Seder, I., Moon, H., Kang, S.J., Shin, S., Rhee, W.J., Kim, S.J., 2022. Lab Chip 22 (19), 3699–3707.
Si, H., Xu, G., Jing, F., Sun, P., Zhao, D., Wu, D., 2020. Sensor. Actuator. B Chem. 318, 130788.
Song, M., Hong, S.G., Lee, L.P., 2023. Adv. Mater. 35 (10), 2207138.
Song, Q., Gao, Y., Zhu, Q., Tian, Q., Yu, B., Song, B., Xu, Y., Yuan, M., Ma, C., Jin, W., Zhang, T., Mu, Y., Jin, Q., 2015. Biomed. Microdevices 17 (64).
Stroock, A.D., Dertinger, S.K.W., Ajdari, A., Mezić, I.M., Stone, H.A., Whitesides, G.M., 2002. Science 295 (555), 647–651.
Strotman, L.N., Lin, G., Berry, S.M., Johnson, E.A., Beebe, D.J., 2012. Analyst 137 (17), 4023–4028.
Sunkara, V., Kumar, S., Sabaté Del Río, J., Kim, I., Cho, Y.K., 2021. Acc. Chem. Res. 54 (19), 3643–3655.
Troiano, D., Deraney, R.N., Tripathi, A., 2017. Colloids Surf. A Physicochem. Eng. Asp. 513, 188–195.
Vos, L.M., Bruning, A.H.L., Reitsma, J.B., Schuurman, R., Riezebos-Brilman, A., Hoepelman, A.I.M., Oosterheert, J.J., 2019. Clin. Infect. Dis. 69 (7), 1243–1253.
Wang, R., Taubenberger, J.K., 2010. Expert Rev. Anti Infect. Ther. 8 (5), 517–527.
Wu, Z., Bai, Y., Cheng, Z., Liu, F., Wang, P., Yang, D., Li, G., Jin, Q., Mao, H., Zhao, J., 2017. Biosens. Bioelectron. 96, 339–344.
Xu, G., Si, H., Jing, F., Sun, P., Zhao, D., Wu, D., 2020. Micromachines 11 (12), 1025.
Xu, L., Wang, A., Li, X., Oh, K.W., 2020. Biomicrofluidics 14 (3), 031503.
Yeh, E.-C., Fu, C.-C., Hu, L., Thakur, R., Feng, J., Lee, L.P., 2017. Sci. Adv. 3, e150164 n. d.

Yin, J., Zou, Z., Hu, Z., Zhang, S., Zhang, F., Wang, B., Lv, S., Mu, Y., 2020. Lab Chip 20 (5), 979–986.
Yu, Z., Lyu, W., Yu, M., Wang, Q., Qu, H., Ismagilov, R.F., Han, X., Lai, D., Shen, F., 2020. Biosens. Bioelectron. 155, 112107.
Zheng, Y., Hu, P., Ren, H., Wang, H., Cao, Q., Zhao, Q., Li, H., Zhang, H., Liu, Zhanxu, Li, Y., Wang, C., Liu, Zengshan, Lu, S., 2021. Anal. Biochem. 621, 114157.
Zhou, X., Ravichandran, G.C., Zhang, P., Yang, Y., Zeng, Y., 2019. Lab Chip 19 (24), 4104–4116.
Zhu, H., Fohlerová, Z., Pekárek, J., Basova, E., Neužil, P., 2020. Biosens. Bioelectron. 153, 112041.